LAWRENCE
LIVERMORE
NATIONAL
LABORATORY

UCRL-JRNL-223584

Temperature sensitivity of Cu K(alpha) imaging efficiency using a spherical Bragg reflecting crystal

K. U. Akli, M. H. Key, H. K. Chung, S. B. Hansen, R. R. Freeman, M. H. Chen, G. Gregori, S. Hatchett, D. Hey, N. Izumi, J. A. King, J. Kuba, P. Norreys, A. J. Mackinnon, C. D. Murphy, R. Snavely, R. Stepehens, C. Stoeckel, W. Theobald, B. Zhang

August 9, 2006

Physics of Plasma

Disclaimer

Temperature sensitivity of Cu K_α imaging efficiency using a spherical Bragg reflecting crystal

K. U. Akli[1,2], M. H. Key[1], H. K. Chung[1], S. B. Hansen[1],
R. R. Freeman[2,3], M. H. Chen[1], G. Gregori[4], S. Hatchett[1], D. Hey[1,2],
N. Izumi[1], J. King[1,2], J. Kuba[7], P. Norreys[4], A. J. Mackinnon[1],
C. D. Murphy[4], R. Snavely[1], R. Stephens[6], C. Stoeckel[5], W. Theobald[5], B. Zhang[2].

[1] *Lawrence Livermore National Laboratory*

[2] *University of California Davis, California*

[3] *The Ohio State University, Ohio*

[4] *Rutherford Appleton Laboratory, United Kingdom*

[5] *University of Rochester, Rochester, New York*

[6] *General Atomics, San Diego, California and*

[7] *Czech Technical University, Prague, Czech Republic*

(Dated: August 7, 2006)

Abstract

The Vulcan laser facility at the Rutherford Appleton Laboratory was used to study the interaction of a 75 J 10 ps, high intensity laser beam with low-mass solid, Cu targets. Two instruments were fielded as diagnostics of the Cu K-shell emission from the targets: A single photon counting CCD spectrometer provided the absolute K_α yield and a spherically bent Bragg crystal recorded 2D monochromatic images with a spatial resolution of 10 μm. Due to the shifting and broadening of the K_α spectral lines with increasing temperature, there is a temperature dependence of the crystal collection efficiency. This provides a temperature diagnostic when cross calibrated against a single hit CCD spectrometer, and it affects measurements of the spatial pattern of electron transport. The experimental data showing changing collection efficiency are presented. The results are discussed in light of modeling of the temperature-dependent spectrum of Cu K-shell emission.

I. INTRODUCTION

The advent of short-pulse laser technology has made it possible to create and explore isochorically heated high energy density matter. With this comes the need for diagnostics to unravel the fundamental physics of these transient plasmas. As plasma diagnostics, spherically bent Bragg crystals have been used in a back-lighter configuration to study the dynamics of laser imploded targets [1], wire-array Z-pinch implosions [2], and ablative Richtmyer-Mashkov instability [3]. They have been used also as diagnostics in the context of fast ignition [4] to get insight into short-pulse, high-energy laser generated electron transport and the associated isochoric heating of the targets [5]. For example, Stephens et al. [6] used a spherically bent Bragg crystal coupled with a CCD to obtain monochromatic spatially resolved 2D images of planar targets with buried Ti or Cu fluor layers. Due to the shifting and broadening of the K_α emission line with temperature [7], care must be taken in interpreting the results, especially when dealing with low mass targets and high laser energies which produce high temperatures. In this paper, we describe a temperature-dependent K_α diagnostic, present the experimental evidence of changing collection efficiency, and discuss it in light of modeling of the temperature dependent Cu K-shell emission.

II. EXPERIMENTAL SETUP

The short-pulse, high intensity beam of Vulcan laser facility at the Rutherford Appleton Laboratory was used to irradiate planar solid Cu foils. This infrared (1.053 μm) laser pulse was generated using the Chirped Pulse Amplification (CPA) technique [8] and contained 75 J of energy delivered in 10 ps. A peak intensity of $\sim 5 \times 10^{18}\ W/cm^2$ was achieved by using an f/3 off-axis parabola to focus the beam to a 10 μm focal spot. About 50% of the laser energy on target was contained in the central spot, the remaining energy is distributed over the wings. The spontaneous stimulated emission (ASE) contrast ratio was 10^{-7} in intensity and 10^{-4} in energy. The targets were planar solid Cu foils of 100 μm x 100 μm and 500 μm x 500 μm lateral dimensions and of varying thicknesses (1 μm to 30 μm). X-rays emitted following K-shell ionization by hot electrons were collected using the following two instruments.

A. Spherically bent Bragg imager

The first instrument is a monochromatic K_α imager, which consists of a spherically bent Bragg crystal coupled to a charge-coupled device (CCD). A Silicon dioxide crystal with a 38 cm radius of curvature, 3.082 $\mathring{A}$ 2d lattice spacing, and 2131 Miller indices was used. This required an incidence angle of 1.3° in order to satisfy the Bragg condition in second diffraction order for Cu K_α at 8 keV. The crystal was located at an object distance of 214 cm resulting in a magnification of 8. The alignment procedure is straightforward and is discussed in details by Koch et al [9]. A 10 μm astigmatism-limited spatial resolution [9] was obtained by putting a 1.6 cm diameter aperture in front of the crystal. The geometrical size of the aperture and the source size determine the bandwidth of the crystal. Assuming a point source the minimum and maximum angles subtended by the rays coming from the source and reflecting at locations adjacent to the aperture edges are 0.37° and 2.22° respectively (Fig. 1). The corresponding energies reflected at these angles are 8.046 keV and 8.052 keV, which gives an aperture energy bandwidth ΔE of 5.8 eV. The crystal viewed the rear side of the target at an angle of 37.8° with respect to the horizontal plane and 32° with respect to the target normal.

The K_α photons were collected with a Princeton Instruments CCD camera, cooled to -20 ° Celsius. The model used was PI-SX1300, which is a high sensitivity back-illuminated digital system with 1340x1300 imaging array, 20 μm pixel size, and 16-bit recording resolution. A 25 μm Cu filter was located in front of the CCD to narrow the bandwidth of the radiation reaching the detector by reducing the number of photons with energies above the Cu K-Shell photoabsorption edge. A typical monochromatic 2D spatially resolved image is shown in Fig. 2 (500 μm x 500 μm 30 μm thick Cu target).

B. Single hit CCD spectrometer

The second instrument used to collect the generated x-rays was a CCD camera operated in the single-photon counting regime. It directly detects photons without the use of any optical elements. For every 3.65 eV of photon energy absorbed silicon a photoelectron is created. When the single photon counting condition is satisfied, the number of photoelectrons created in a single pixel is a direct measurement of the energy of the absorbed photon. In Si the

absorption of a Cu K_α photon (8.048 keV) will create around 2205 photoelectrons. The ability of CCD's to operate in this mode has been demonstrated for example by Schwartz et al [10], Yasuike at al [11], Stoeckl et al [12]. We used an SI 800-145 back-illuminated CCD camera manufactured by Spectral Instrument-Photonics. This camera has a 5% quantum efficiency at 8 keV for single hits with negligible spread of the absorbed x-rays energy over adjacent pixels [13]. It was located at a distance of 1.4 m from the target and surrounded with lead shielding to protect it from hard x-ray background and high-energy particles generated in the target chamber [12]. The photons were detected from the front side of the target at an angle of 16° with respect to the target normal [13].

III. MEASUREMENTS OF THE K_α YIELD

The data from the imager were processed and analyzed using the Interactive Data Language (IDL), a product of Research Systems, Inc. (RSI). Background images were taken in the same environment minutes before each shot with the CCD cooled to -20 C and the filter in front of the array. The background images are then subtracted from the data images pixel by pixel. The hard hits resulting from high energy photons and particles interacting with the detector are removed from the images by applying a smoothing routine, whereby the value of a pixel is substituted by that of the median of its neighbors, if its value is higher by 10% or more than that of the median of the neighbors. The yield of K-shell emission from the target was then determined by integrating the images. The associated relative standard error was very small (0.2%-1.2%) due to the large number of photons detected .

A histogram or pulse-height-distribution of the pixel values of the single-hit CCD spectrometer allows extracting the x-ray spectrum. The absolute number of K_α yield was then determined by summing the number of hits contained in the K_α-line shape and by taking the solid angle, filter transmission, and quantum efficiency of the CCD in single-pixel analysis mode into account [14]. An isotropic emission into a 4π steradians solid angle is assumed.

The FWHM spectral line width was determined to be 220 eV at ~ 8 keV leading to a spectral resolution of $E/\Delta E = 37$. The integral fractional number of exposed CCD pixels with Cu K-shell energy is $\sim 0.3\%$, but a significant number of pixels ($< 40\%$) are exposed to low energy events below 5 keV, which might be generated by a fractional deposition from high energy x rays and fluorescence radiation from the inside of the CCD chamber walls.

The total amount of CCD image exposure influences the calculation of the line yield and has been taken into account by the method described in Ref. [13]. Within the low level of Cu K-shell emission pixel exposure, the CCD is operating in a single-photon-counting mode. The relative error bars are estimated to be $\sim 40\%$ based on the standard deviation of several measurements at the same experimental condition. The absolute uncertainty is estimated to be a factor of 2.4 based on an estimated uncertainty in the CCD quantum efficiency for single-pixel analysis [14] and the relative measurement error.

The Cu K_α yield obtained from both instruments is normalized to the total laser energy on target and plotted as a function of the target volume (Fig. 3). The line with diamonds indicates the total amount of Cu K_α emission collected by the single hit CCD spectrometer in absolute units (ph/sr/J). The line with x's shows the amount collected by the crystal imager in arbitrary units (a.u). With decreasing target volume, it is clear that the yield obtained from the crystal imager decreases faster than the yield from the single hit spectrometer. This effect, attributed to the temperature-induced line shifting and broadening, is more pronounced for small targets which attain high temperatures. In principle this reduction in the yield can be used as an independent temperature diagnostic when cross calibrated with the single-hit CCD spectrometer. The data point on the top right corner is from a 500 μm x 500 μm 30 μm thick target. The remaining three data points are from 100 μm x100 μm targets with thicknesses of 1 μm, 5 μm, and 20 μm respectively.

IV. SPECTROSCOPIC MODELLING OF THE K-SHELL EMISSION

Accurate and complete modelling of K-shell emission from multiply-ionized Cu ions immersed in hot, dense plasma is difficult due to the large number of states that must be included. Apart from the complexity of the level structure, the collisional radiative kinetics cannot be treated in the standard single temperature way, since the thermal electrons that control the distribution of charge states in the M-shell have insufficient energy to participate in the inner-shell processes which produce K-alpha emission. Thus collisional rates must be calculated using non-thermal electron energy distributions. The change in the ionic potential under valence-shell ionization by the bulk thermal electrons leads to a shifting and broadening of the K_α emission feature. Modelling of this line shifting and broadening as a function of the plasma temperature was carried out using two atomic codes: the flexible

atomic code (FAC) [15] and the generalized population kinetics model FLYCHK [16]. We first used FAC to compare spectra from detailed level (DL) and configuration-average (CA) models in order to test the accuracy of the CA model used later in FLYCHK for spectral synthesis.

Fig. 4 shows comparisons of spectra calculated using Local Thermodynamic equilibrium populations (LTE) in detailed level (DL) and configuration-average (CA) models. We have verified the statistical assumption using the collisional-radiative model SCRAM [17]. The data for each model was calculated using FAC in either standard (detailed fine structure) or unresolved-transition-array (UTA) mode. The two plots show the comparison of DL and CA with varying degrees of completeness in level structure. The plot on the top includes about 21 fine structure levels in the DL model of Ar-like Cu. The central plot includes about 9000 levels. The CA models for the two cases have 9 and 160 relativistic averaged levels respectively. The CA spectra are plotted with an imposed transition energy shift of -15 eV to match the predictions of the simplest DL model and are given both with and without including the UTA transition widths. While the energies of CA transition arrays within the dashed-lines envelopes are not perfectly coincident with corresponding features in the DL spectra, the centroids and overall widths of the CA features are in reasonable agreement. Therefore, for the purpose of this paper, it is adequate to use the CA model which reduces the model complexity.

In order to compute the K line shifts and broadening at a given thermal electron temperature, FLYCHK first computes the level population in the super-configuration model and generates emission spectra in the configuration-average (CA) model kinetics, and then FLYSPEC calculates spectra based on CA atomic data from Mau Chen's DHS code [18, 19]. FLYSPEC predictions for Ar-like Cu are in good agreement with the FAC-based CA calculations (see Fig. 4). In our experiment the hot electron temperature was about 600 keV as estimated, from the laser intensity, using Beg's scaling law [20]. The hot electron density was in the range of 10^{-4} to 10^{-3} of the total electron density. This estimate is based on experimental laser-to-electron conversion efficiency [21] and Cu K_α spot size [6]. The total electron density is computed self-consistently by the solid ion density times the mean charge state. While the absolute K_α intensity is a function of hot electron temperature and density, the spectral shape is rather insensitive to them and depends on the thermal electron temperature as long as the fraction of hot electrons is less than 10% of total electron density,

which is the case in our experiment. The calculated spectra are plotted in Fig. 5 (red line) for thermal electron temperatures ranging from 1 eV to 300 eV. Also plotted is the energy bandwidth of the crystal centered at 8.048 keV.

V. COLLECTION EFFICIENCY OF THE BRAGG CRYSTAL IMAGER

The Cu K_α emission line, in addition to broadening, exhibits a negative shift at first as shown by the peak moving to the left (Fig. 5). As the plasma temperature increases, the broadening increases and the energy shifts become positive. The ratio of the area under the curve bounded by the crystal reflectivity bandwidth to the total area under the curve is proportional to the collection efficiency of the crystal. In the calculation of the collection efficiency $\epsilon(T)$ a normalization factor was applied. The chosen normalization made the collection efficiency 100% when the target is cold ($T \approx 1eV$). Fig. 6 (dashed line) shows that $\epsilon(T)$ is a decreasing function of temperature. ϵ has a value between 50% to 100% only in a small interval 1 - 20 eV; above 20 eV the efficiency is significantly reduced.

Due to the time-integrated nature of the diagnostic, the amount of radiation collected by the imager at a given time is proportional to the collection efficiency at that time and therefore the temperature. If $Y(T)$ is the K_α yield from a $1\mu m$ solid density Cu slab at temperature T, then the yield collected by the imager at this temperature is $Y(T)\epsilon(T)$. The total yield collected when the slab is heated from T_0 to T_{max} is, therefore, given by the following integral,

$$\int_{T_0}^{T_{max}} Y(T)\epsilon(T)\ dT \tag{1}$$

The above integral quantity is shown in Fig. 6 (solid line with x's). It increases rapidly with temperature and reaches a plateau at about 100 eV. One of the implications of this temperature-dependence of the collection efficiency is the saturation of the amount of photons collected. This effect will impose limitations on the use of spherically bent Brag crystals as diagnostics for very hot plasmas. The dashed line with open squares in Fig. 6 shows the reduction in the cumulative yield as function of the final temperature of the slab. Increasing the temperature from 0 to 50 eV results in 50% reduction in the collected yield.

VI. NUMERICAL MODEL

The temperature throughout the target is not constant but rather decreases with depth and radial distance from the laser focal spot. Furthermore, the interaction of the laser beam with the target is local and time varying. To account for these two effects in interpreting our data, a numerical model was developed.

The calculations are carried out in cylindrical geometry. We start with modelling the laser pulse using the following double Gaussian profile, based on the experimentally measured focal spot,

$$I_{Laser}(r,t) = \frac{1}{2}\ I_{peak}\ \exp\left[-\left(\frac{t-t_p}{\tau}\right)^2\right]\left\{\ \exp\left[-\left(\frac{r}{R_1}\right)^2\right] + \exp\left[-\left(\frac{r}{R_2}\right)^2\right]\right\} \qquad (2)$$

here $R_1 = 5\mu m, R_2 = 10\mu m$, $I_{peak} = 5 \times 10^{18}\ W/cm^2$, $t_p = 5ps$, and $\tau = 2.5ps$.
The hot electrons generated by the interaction of this pulse with the target are described by a local Maxwellian distribution,

$$f_E(E,r,t) \propto \frac{\sqrt{E}}{T_h(r,t)^{3/2}} \times \exp\left[-\frac{E}{T_h(r,t)}\right] \qquad (3)$$

where the local temperature, $T_h(r,t)$, is given by Beg's scaling law [20].
The number of hot electrons in each zone of radius r is calculated from their local total energy and their mean energy. Their mean energy is simply $\frac{3}{2} \times T_h(r,t)$. Their local total energy is $\eta_L \times E_{Laser}(r,t)$, where η_L is an intensity dependent laser-to-electrons conversion efficiency taken from Key et al. [21]. The calculations are carried out in concentric cylindrical zones of radii r and length Δz. Although this approach ignores electron scattering, it accounts for electron resistive inhibition [22, 23] for thick targets and refluxing [13, 24] for thinner ones.

For thick targets, the temperature in each zone, $T(r,z,t)$, is determined from the specific energy deposited using LANL SESAME equation of state tables. The energy deposited has two components: collisional and Ohmic. The contribution of collisions is determined using the stopping power of electrons in hot plasmas from refefrence [25, 26],

$$\frac{dE}{ds} = -\frac{2\pi r_0^2 mc^2 n_i Z}{\beta^2} \times \left[\ln\left[\frac{(\gamma-1)\lambda_D}{2\sqrt{2\gamma}r_0}\right]^2 + 1 + \frac{1}{8}\left(\frac{\gamma-1}{\gamma}\right)^2 - \left(\frac{2\gamma-1}{\gamma}\right)\ln 2 + \ln\left(\frac{1.123\beta}{\sqrt{2kT_h/mc^2}}\right)^2\right] \qquad (4)$$

The Ohmic component is proportional to the square of the neutralizing return current density. For $T(r,z,t) < 100$ eV the resistivity is approximated by its maximum value of $10^{-6}\Omega$ m at the plateau [27] and above 100 eV the Spitzer resistivity is used. In each step the influence of the potential on the energy of the electrons is accounted for. The return current density is given by the following expression:

$$\overrightarrow{j}_{return}(r,z,t) \approx -\overrightarrow{j}_{fast}(r,z,t) = e \int c\ \beta(E)\ n_h(r,z,t,E)\ dE\ \frac{\overrightarrow{z}}{\|\overrightarrow{z}\|} \tag{5}$$

where $n_h(r,z,t,E)\ dE$ is the number of hot electrons per unit volume with energies between E and $E + dE$ in a zone with given (r,z) at time t.

For thin targets the situation is different. The electrons traverse the target and set up an electrostatic sheath of thickness of the order of Debye length. The sheath was characterized by the electric field strength of order $T_h(r,t)/e\lambda_D$. The Debye length, λ_D, is a function of the electron density and temperature. These last two quantities are functions of time. Therefore the potential which is the product of electric field strength and Debye length is also a function of time. The first electrons created by the leading edge of the laser pulse at earlier time establish a sheath with a potential $\varphi(t_0)$. This potential is not strong enough to influence the electrons. The incoming electrons at later time increase the magnitude of the potential due to more charge separation. In the calculation, this potential is evaluated as a function of time. When the value of $\varphi(t)$ is equal to their mean energy, electrons coming at that time reflect from the rear surface. These electrons are also reflected from a similar Debye sheath at the front surface. The process is repeated for the lifetime of the electrons, hence the name "refluxing". The first electrons establishing the sheath are not circulated. The specific energy deposited in the target is due to collisions only, the electrons act as their own return current by virtue of refluxing.

The distribution, $N_{ph}(r,z,t)$, of K_α photons induced by these electrons is then calculated according to,

$$N_{ph}(r,z,t) = \int n_{Cu}\ \Delta z\ \sigma(E)\ N_h(r,z,t,E)\ dE \tag{6}$$

where $N_h(r,z,t,E)\ dE$ is the number of hot electrons with energies between E and $E + dE$ in the zone, n_{Cu} is the copper number density, and $\sigma(E)$ is the electron impact ionization cross section in Cu. For $\sigma(E)$ we used the Deutsch-Mark expression,

$$\sigma(E) = 2\pi\ r_{1s}^2\ g_{1s}\ f\left(\frac{E}{E_{1s}}\right)\ F\left(\frac{E}{E_{1s}}\right) \tag{7}$$

where r_{1s} is the radius of maximum radial density of Cu 1s-shell from the tables of Desclaux [28], g_{1s} is a weighting factor, E_{1s} is the binding energy of 1s electrons, and the functions f, F are those in reference [29].

VII. DISCUSSION AND SUMMARY

Using the model described above both the local and total K_α yields were determined. The total number of photons per steradian from the target is given by the following integral,

$$N_T = \frac{1}{4\pi} \int \int \int N_{ph}(r, z, t) \exp -\{\mu(s - z)\} \; dt \; dz \; dr \tag{8}$$

here μ is the attenuation coefficient of K_α radiation in Cu. N_T is plotted as a function of the target volume in Fig. 7 (dashed line with triangles). It is in good agreement with the experimental data from the single hit CCD spectrometer (solid line with diamonds). The experimental yield from the 1 μm thick target is little lower than the modelled. The reason for this may be that the electrons lose their energy to channels other than electron impact ionization (pdV work accelerating protons for example). When the previously determined collection efficiency correction is applied, the total number of photons per steradian collected by the imager is reduced to:

$$N_{T_r} = \frac{1}{4\pi} \int \int \int N_{ph}(r, z, t) \exp -\{\mu(s - z)\} \; \epsilon(r, z, t) \; dt \; dz \; dr \tag{9}$$

where $\epsilon(r, z, t)$ is the local collection efficiency.
N_{T_r} is plotted in Fig. 7 (dashed line with open squares). Also plotted are the experimental data from the imager (solid line with x's). The value of N_{T_r} for the 30 μm thick target was used as a normalization point for the experimental data since these data were not measured in absolute units. The thickest target was chosen based on the fact that it is the least susceptible to temperature effects. Both the modelled and experimental results are in a good agreement, showing the temperature-dependence of the collected K_α yield. The total yield was reduced by a factor of 2 for the thickest target and by a factor of 17 for the thinnest one.

Finally, as an example, the model is applied to the spatial pattern of K_α intensity for the 30 μm thick target. A useful approach in analyzing 2D spatially resolved images is a lineout through the image. Such a lineout is plotted in Fig. 8 (dashed line with triangles).

It was taken in the horizontal direction through the middle of the K_α image of Fig. 2. The dashed line is the modelled lineout with the line shifting and broadening taken into account. The solid line is the true lineout that one should expect if the imager were not susceptible to temperature effects. the reduction was almost uniform ranging from 62% in the center to 56% at the edges. As consequence the full width at half maximum remained unchanged while the brightness of the image is reduced. For thinner targets, the reduction was more pronounced at the center than the edges. This resulted in an apparent increase in the FWHM. Neglecting these effects when interpreting data will lead to erroneous results for the FWHM more so in case of high temperatures.

In summary, experimental evidence of temperature sensitivity of Cu K_α imaging efficiency using a spherical Bragg reflecting crystal was presented. The experimental data were interpreted using two models. First, the temperature-dependent spectrum of Cu K-shell emission was modeled using FLYCHK in the configuration-average (CA) mode. Then, a numerical transport model which takes into account the electron refluxing was used to obtain both the absolute K_α yield and the spatial pattern of K_α intensity. It was found that both the brightness and the pattern of K_α intensity are affected by the rise of the target temperature.

Acknowledgments

We wish to acknowledge the support of R. Heathcote, P. Brummitt, D. Neville, and M. Tolley. This Work was performed under the auspices of the U.S. Department of Energy by the Lawrence Livermore National Laboratory under Contract No. W-7405-ENG-48.

This work was performed under the auspices of the U.S. Department of Energy by University of California, Lawrence Livermore National Laboratory under Contract W-7405-Eng-48.

[1] J. A. King, Rev. Sci. Instrum **76**, 076102 (2005).

[2] D. B. Sinars, Rev. Sci. Instrum **74**, 2202 (2003).

[3] J. A. Aglitsky, Phys. Rev. Lett **87**, 265001 (2001).

[4] M. Tabak, Phys. Plasmas **1**, 1626 (1994).

[5] M. H. Key, Inertial Fusion Sciences and Applications (IFSA) (2003).

[6] R. B. Stephens, Phys. Rev. E **69**, 066414 (2004).

[7] G. Gregori and S. B. Hansen, Contrib. Plasma Phys **45**, 284 (2005).

[8] D. Strickland and J. Mourou, Opt. Commun **56**, 219 (1985).

[9] J. A. Koch, Rev. Sci. Instrum **74**, 2130 (2003).

[10] D. A. Schwartz, Proc. SPIE **184**, 247 (1979).

[11] K. Yasuike, Rev. Sci. Instrum **72**, 1236 (2001).

[12] C. Stoeckl, Rev. Sci. Instrum **75**, 3705 (2004).

[13] W. Theobald, Phys. Plasmas **13**, 043102 (2006).

[14] H. S. Park, Phys. Plasmas **13**, 056309 (2006).

[15] M. F. Gu, AIP Conference Proceedings **730**, 127 (2004).

[16] H. K. Chung, High Energy Density Physics (HEDP) **1**, 3 (2005).

[17] S. B. Hansen, Ph.D. thesis, University of Nevada, Reno (2003).

[18] M. H. Chen, Phys. Rev. A **31**, 556 (1985).

[19] K. N. Huang, At. Data and Nucl. Data Table **18**, 243 (1976).

[20] F. N. Beg, Phys. Plasmas **4**, 447 (1997).

[21] M. H. Key, Phys. Plasmas **5**, 1966 (1998).

[22] A. R. Bell, Plasma Phys. Controlled Fusion **39**, 653 (1997).

[23] D. J. Bond, Phys. Rev. Lett **42**, 252 (1980).

[24] A. J. Mackinnon, Phys. Rev. Lett **88**, 215006 (2002).

[25] C. K. Li, Phys. Rev. E **70**, 067401 (2004).

[26] C. K. Li, Phys. Rev. E **73**, 016402 (2006).

[27] H. M. Miltchberg, Phys. Rev. Lett **62**, 2364 (1988).

[28] J. P. Desclaux, Atom. Data Nucl. Data Tables **12**, 325 (1973).

[29] H. Deutsch, International Journal of Mass Spectrometry **213**, 5 (2002).

Figure Captions

FIG. 1. Cartoon showing spherically bent Bragg crystal. The minimum and maximum angles θ_{min} and θ_{max} satisfying the Bragg condition in second order are 0.37° and 2.22° respectively. The energies reflected at these angles are 8.046 KeV and 8.052 KeV.

FIG. 2. A typical monochromatic 2D spatially resolved Cu K_α image. The target is a 500 μm x 500 μm 30 μm thick Cu foil.

FIG. 3. Cu K_α yield: diamonds, the absolute Cu K_α emission (ph/sr/J) measured by the single hit CCD spectrometrer. x's, the integral K_α emission from the crystal imager in arbitrary units (a.u).

FIG. 4. Comparison of model predictions for K-shell emission from Ar-like Cu. The spectra change significantly as the number of modeled configurations is increased (top to bottom). Configuration-averaged (CA) models show reasonable agreement with detailed-level (DL) models when transition energy shifts δE and UTA widths σ^{UTA} are included.

FIG. 5. FLYCHK spectra for temperatures ranging from 1 eV to 300 eV. The two vertical black lines indicate the maximum and minimum energies reflected by the crystal.

FIG. 6. Dashed line with triangles, the crystal imager collection efficiency as a function of target temperature. Solid line with x's, total K_α yield when the slab is heated to temperature T. Dashed line with open squares, the reduction in the cumulative yield as function of the final temperature T of the slab.

FIG. 7 Comparison of the experimental and modeled absolute K_α yields. Experimental: solid line with diamonds from the single hit CCD, solid line with x's from the crystal imager normalized as discussed in the text. Modeled: dashed line with squares, the yield from the imager with temperature effects. dashed line with triangles, the absolute yield.

FIG. 8. Cu K_α spatial pattern of intensity: solid line with triangles, a horizontal li-

neout of the image of the 500 μm x 500 μm 30 μm thick target in Fig. 2. Solid line, model lineout with no temperature effects. Dashed line, model lineout with temperature effects.

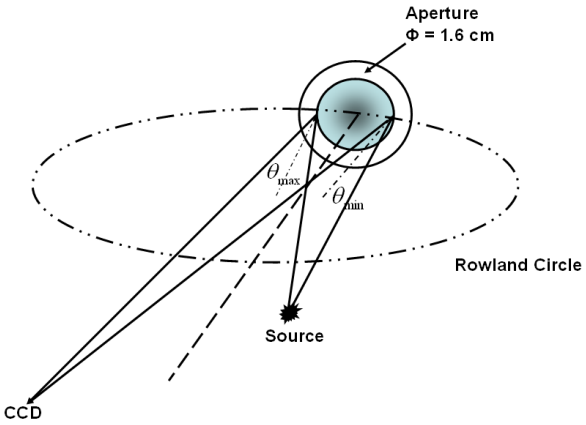
Aperture
Φ = 1.6 cm
θ_{max}
θ_{min}
Rowland Circle
Source
CCD

FIG. 1:

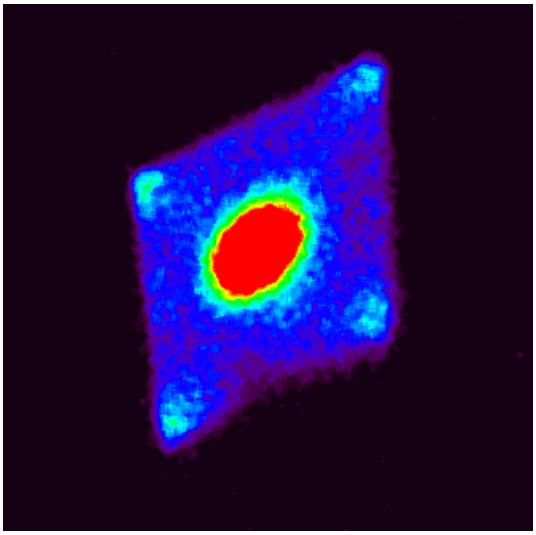

FIG. 2:

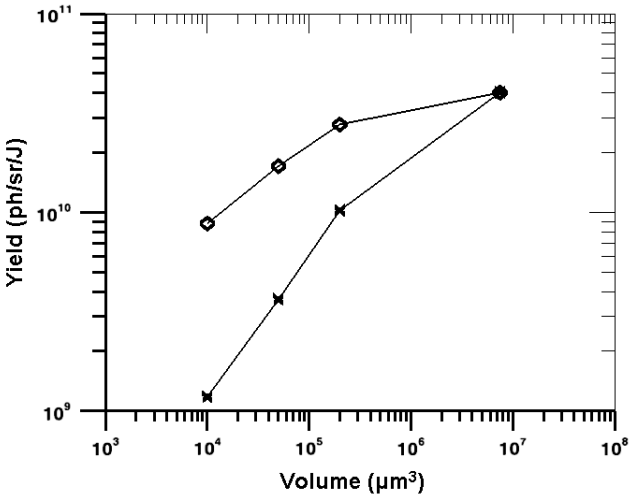

FIG. 3:

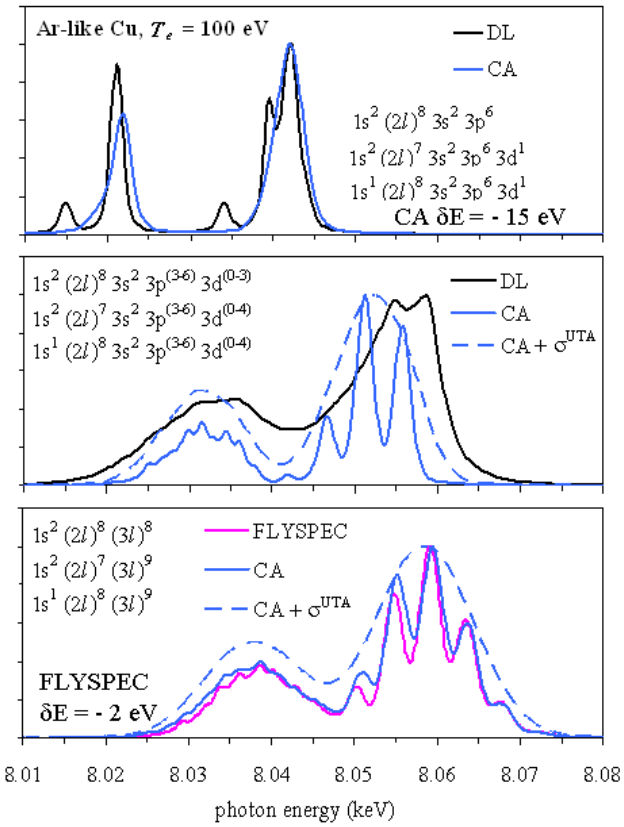
Ar-like Cu, T_e = 100 eV
DL
CA
$1s^2\,(2l)^8\,3s^2\,3p^6$
$1s^2\,(2l)^7\,3s^2\,3p^6\,3d^1$
$1s^1\,(2l)^8\,3s^2\,3p^6\,3d^1$
CA δE = - 15 eV
$1s^2\,(2l)^8\,3s^2\,3p^{(3-6)}\,3d^{(0-3)}$
$1s^2\,(2l)^7\,3s^2\,3p^{(3-6)}\,3d^{(0-4)}$
$1s^1\,(2l)^8\,3s^2\,3p^{(3-6)}\,3d^{(0-4)}$
DL
CA
CA + σ^{UTA}
$1s^2\,(2l)^8\,(3l)^8$
$1s^2\,(2l)^7\,(3l)^9$
$1s^1\,(2l)^8\,(3l)^9$
FLYSPEC
CA
CA + σ^{UTA}
FLYSPEC
δE = - 2 eV
8.01
8.02
8.03
8.04
8.05
8.06
8.07
8.08
photon energy (keV)

FIG. 4:

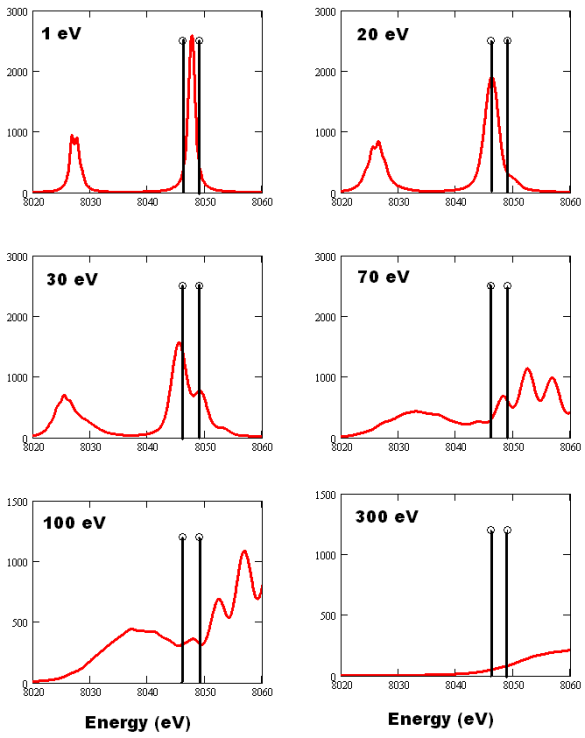

FIG. 5:

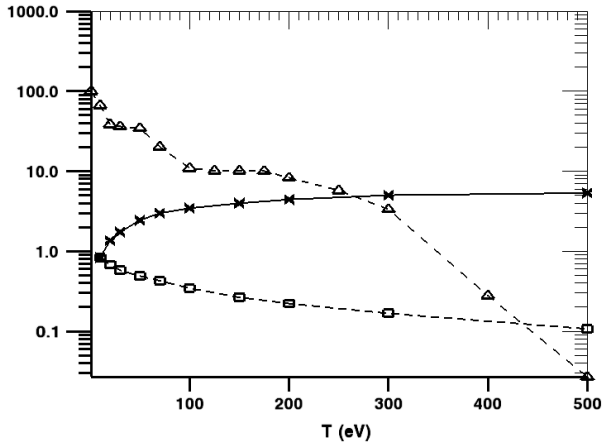

FIG. 6:

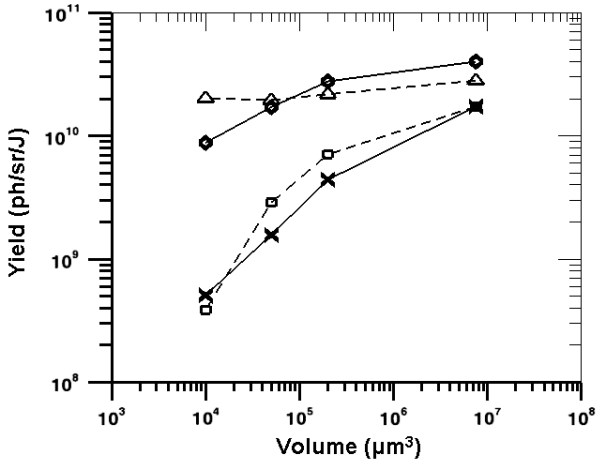
Yield (ph/sr/J)
Volume (μm³)
10¹¹
10¹⁰
10⁹
10⁸
10³
10⁴
10⁵
10⁶
10⁷
10⁸

FIG. 7:

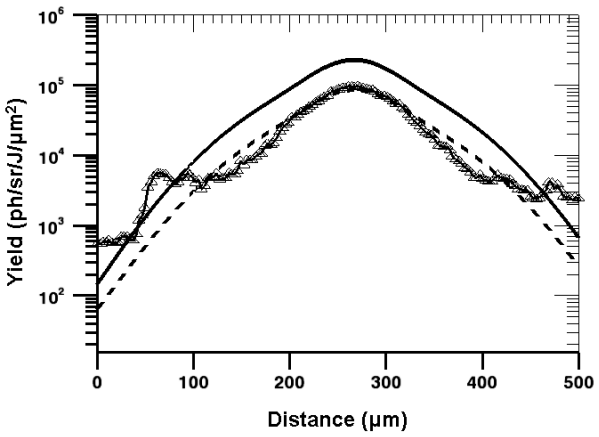
Yield (ph/sr/J/μm²)
10⁶
10⁵
10⁴
10³
10²
0
100
200
300
400
500
Distance (μm)

FIG. 8: